J Mater Sci (2018) 53:1945–1961

Composites

Preparation and self-assembly of Au nanoparticles coordinated Fe_3O_4 graft block copolymer multifunctional nanohybrids with pH, electrochemical and magnetic stimuli responsiveness

Jing-Wen Xu[1], Zhuo-Miao Cui[1], Feng Xu[1,*], and Yan-Ling Luo[1,*]

[1] *Key Laboratory of Macromolecular Science of Shaanxi Province, School of Chemistry and Chemical Engineering, Shaanxi Normal University, Xi'an 710062, People's Republic of China*

Received: 8 July 2017
Accepted: 5 October 2017
Published online: 12 October 2017

ABSTRACT

Multi-component block copolymer nanohybrids consisting of Fe_3O_4 nanoparticles and poly(acryloyloxyethyloxyl 1-mercaptohemisuccinate) and poly (methacrylic acid) (PMAA) blocks were synthesized via the surface-initiated atom transfer radical polymerization, followed by the esterification with d,l-mercaptosuccinic acid. The block copolymer nanohybrids were coordinated with Au nanoparticles (Au NPs) through pendent thiol groups to form Au NPs coordinated Fe_3O_4 graft block copolymer nanohybrids. Fluorescent spectrometry, TEM and SEM findings indicated that these block copolymer nanohybrids could self-assembled and form globular core–shell nanomicelles, and their critical micelle concentrations decreased with the decrease in the length of PMAA chains and the incorporation of Au NPs. *Zeta* potential measurements signified that the copolymer nanohybrids possessed significantly high stability. DLS results indicated that hydrodynamic diameters of the copolymer nanohybrids distributed within the scope of 85–155 nm, hinging on the length of the graft chains and the complexation of Au NPs. The hybrid block copolymer nanomicelles exhibited pH, electrochemical and magnetic responsiveness, with pH transition points at 5.3–5.9. The incorporation and the loading percentage of Au NPs improved the reversibility of the electrochemical response and plasmon resonance. The block copolymer nanohybrids were superparamagnetic and were expected to broaden their applications by virtue of the multi-component combination and the resulting multifunctionality.

Address correspondence to E-mail: fengxu@snnu.edu.cn; luoyanl@snnu.edu.cn

DOI 10.1007/s10853-017-1675-4

Introduction

With the increasing development of applied technologies and world economies, single systematic materials cannot often meet the requirements for applications, and hence higher demands are put forward for the properties of materials. At present, design and development of new materials with multifunctionality has become the research focuses and attracted broad interests [1–3]. Polymer composites are generally referred to a heterogeneous system that is compounded of various materials, which exhibits designability, anisotropy and combined effect of the properties, such as special additivity, productness, modularity and seepage behavior [4, 5]. This has a very important enlightening and guiding significance for the development of new organic–inorganic hybrid composites. This class of multifunctional materials will possess entirely new functionality in that they have combined two or more components with different properties, and thus greatly broaden their application ranges [6–8]. In particular, for drug delivery systems, it is urgent to develop a new multi-stimuli-responsive 'intelligent' material to accommodate complex circumstances at cancer cells, for example high temperature (> 37 °C), acidic pH (4.8–7.1) and high content of ROS in comparison with normal cells [9, 10]. These extracellular tumor microenvironments provide strategies for increasing tumor selectivity and more effective drug delivery by a synergetic effect.

Fe_3O_4 nanoparticles (Fe_3O_4 NPs) possess unique superparamagnetism, large specific surface area and simple preparation technology [11, 12]. They can potentially be used in batteries, electromagnetic interference shielding, electromagneto-rheological fluids, microwave-absorbing materials, magnetic separation, electrochemical display and recording devices, and sensing [13, 14], as well as some emerging areas such as lithography and biomedicines including enzyme immunoassay, drug targeting delivery and medical diagnosing [15–17]. Consequently, studies on Fe_3O_4 NPs have aroused much enthusiasm and become one of the hottest topics in the fields of nanoscience. Gold nanoparticles (Au NPs) have attracted high attention because of its special optical, electrical, magnetic and catalytic properties including good conductivity, high surface-to-volume ratio, useful electrocatalytic activity toward numerous chemical species and surface plasmon oscillation [18, 19] Au NPs are the most stable metal nanoparticles and extensively applied in biological analysis, biomedical testing, anticancer drugs, drug delivery, sensors, catalysis, antioxidants, larvicides, antimicrobials, nanofluids and agriculture [20, 21]. The combination of Fe_3O_4 NPs with Au NPs can construct new composites with some appealing magnetic and optical characteristics based on their cooperative effects [22, 23]. Moreover, Au NPs as shells can prevent Fe_3O_4 NPs from being oxidized and provide a platform for the follow-up modification [23, 24]. This in turn brings about their potential applications in the fields of magnetofluids, magnetic separation, catalysis, magnetic resonance imaging (MRI), biological technology/biomedicine including detection of cancer cells, magnetic/plasmonic photothermal malignant cell killing, multimodal cancer imaging, dual mode magnetic resonance and chemo-/thermo-therapy, etc. [23–25].

Amphiphilic block copolymers have found wide applications in drug delivery systems (DDS) because of their unique physicochemical properties and high solubility for hydrophobic anticancer drugs [26, 27]. In particular, stimuli-responsive block copolymers can ease the untimely burst release of drug, improve drug enrichment at specific sites, preclude toxic side effects and realize targeted and controlled release of anticancer drugs [28]. When the block copolymers are decorated with Fe_3O_4/Au NPs, an entirely new organic–inorganic hybrid may be constructed, which therefore offer excellent properties from both constituents, soft organic and hard inorganic materials, for example, tailorable mechanical properties, flexibility, processability and microphase separation of organic materials, as well as optical, electrical, catalytic and magnetic properties of inorganic materials, even unknown property profiles [1]. In particular, the organic combination of Fe_3O_4 and Au NPs with tiny nanoparticle size and large specific surface area and stimuli-responsive block copolymers can construct new drug delivery systems that simultaneously possess thermal-, pH-, redox-, magnetic- and/or photo-responsivity [27]. This therefore provides exciting opportunities and opens new avenues for design and development of innovative materials. However, to our knowledge, only finite studies were reported [24, 25]. Consequently, it is highly necessary to engineer and construct new organic–inorganic

nanohybrids with unique architecture and properties to broaden their applications.

In this context, we aim to anchor or graft an amphiphilic block polymer consisting of poly(acryloyloxyethyloxyl 1-mercaptohemisuccinate) (PMSEA) and poly(methacrylic acid) (PMAA) blocks onto the surface of Fe_3O_4 NPs via a surface-initiated atom transfer radical polymerization, followed by the esterification with d,l-mercaptosuccinic acid. The copolymer nanohybrids were complexed with Au NPs through pendent thiol groups to form Au NPs coordinated Fe_3O_4 graft copolymer nanohybrids, Fe_3O_4-*g*-PMSEA@Au-*b*-PMAA. This new organic–inorganic hybrid with unique structure can endow magnetic responsive Fe_3O_4 NPs with stability in aqueous solution, and meanwhile exhibit pH-triggered responsivity, magnetic and electrochemical properties, and plasmon resonance. The effective combination and tailoring of these multi-component systems are anticipated to significantly improve the physicochemical properties, to produce a synergistic effect and to find wide applications.

Experimental section

Materials and reagents

$FeCl_3{\cdot}6H_2O$ (analytically pure, 99%), $FeCl_2{\cdot}4H_2O$ (analytically pure, 99.95%), 2-bromoisobutyryl bromide (BIB, 98%), (3-aminopropyl)triethoxysilane (APTES, 99%), 2-hydroxyethyl acrylate (HEA, 97%), d,l-mercaptosuccinic acid (MSA, 98%), *N*,*N*,*N*′,*N*″,*N*″-pentamethyldiethylenetriamine (PMDETA, 98%), 1-(3-dimethylaminopropyl)-3-ethylcarbodiimide hydrochloride (EDC, 98.5%), 4-dimethylaminopyridine (DMAP, 99%) and $HAuCl_4{\cdot}3H_2O$ (Au ≥ 48%) were offered by Shanghai Macklin Biochemical Co., Ltd., China, and used as received. CuBr (99%, Aladdin Industrial Corp., Shanghai, China) was recrystallized and dried in vacuum. *p*-Toluenesulfonic acid (98%, Acros Organic, USA), tert-butyl methacrylate (*t*BMA, > 98%, TCI) and *p*-methylbenzene sulfonic acid (PTSA, > 98%, Sinopharm Chemical Reagent Co. Ltd., Shanghai, China) were directly used without further purification. Ammonium hydroxide (NH_4OH, 25–28 wt%), triethylamine (TEA, ≥ 99.0%), tetrahydrofuran (THF, ≥ 99.0%), dimethyl sulfoxide (DMSO, ≥ 99.0%), methanol (≥ 99.5%), ethanol (≥ 99.7%), dichloromethane (DCM, ≥ 99.5%) and toluene (≥ 99.5%) were purchased from Sinopharm Chemical Reagent Co. Ltd., Shanghai, China. All solvents were distilled to remove the moisture before use.

Synthesis procedure

Synthesis of Au NPs coordinated Fe_3O_4 graft poly(acryloyloxyethyloxyl 1-mercaptohemisuccinate)-*block*-poly(methacrylic acid) (Fe_3O_4-*g*-PMSEA@Au-*b*-PMAA) was carried out as per an eight-step strategy, as presented in Scheme 1.

Preparation of Fe_3O_4 superparamagnetic nanoparticles (Fe_3O_4 NPs)

The preparation of Fe_3O_4 superparamagnetic nanoparticles (Fe_3O_4 NPs) was performed as per a previous literature [29]. Briefly, $FeCl_3{\cdot}6H_2O$ (8.0 g) and $FeCl_2{\cdot}4H_2O$ (3.6 g) was dissolved in deionized water (64 ml), and then the mixture solution was transferred to a 250-ml four-neck flask under nitrogen atmosphere with fierce stirring. Afterward, NH_4OH (56 ml, 25%) was dropwise added into the reaction system through constant pressure funnel until pH reached about 11. The reaction lasted for 6 h at 50 °C. The resultant mixture was cooled in an ice bath, centrifuged and rinsed with deionized water and ethanol for several times till the pH of the solution reached about 7. The black precipitates were dried in a vacuum box at 40 °C for 24 h to obtain Fe_3O_4 NPs (mean yield: 75%).

Amination of Fe_3O_4 NPs

Fe_3O_4 NPs (1.0 g) were ultrasonically dispersed in anhydrous ethanol (100 ml) in a 250 round bottle flask for 1 h, and then NH_4OH (8 ml, 25%) was blended in the flask. The mixture solution was further ultrasonicated for 20 min. After silane coupling agent APTES (8 ml) was added into the solution, the reaction system was transferred into a 60 °C oil bath, and retained for 48 h under the protection of nitrogen atmosphere, with vigorous churning. Aminated Fe_3O_4 NPs (Fe_3O_4–NH_2 NPs) were centrifuged at 6000 rpm, and cleaned with deionized water and ethanol until pH was about neutral, and dried in vacuo at room temperature for 24 h. The content of amino groups was measured to be 25.0 mmol g^{-1} by potentiometric titration method (details were described in supporting information) [30].

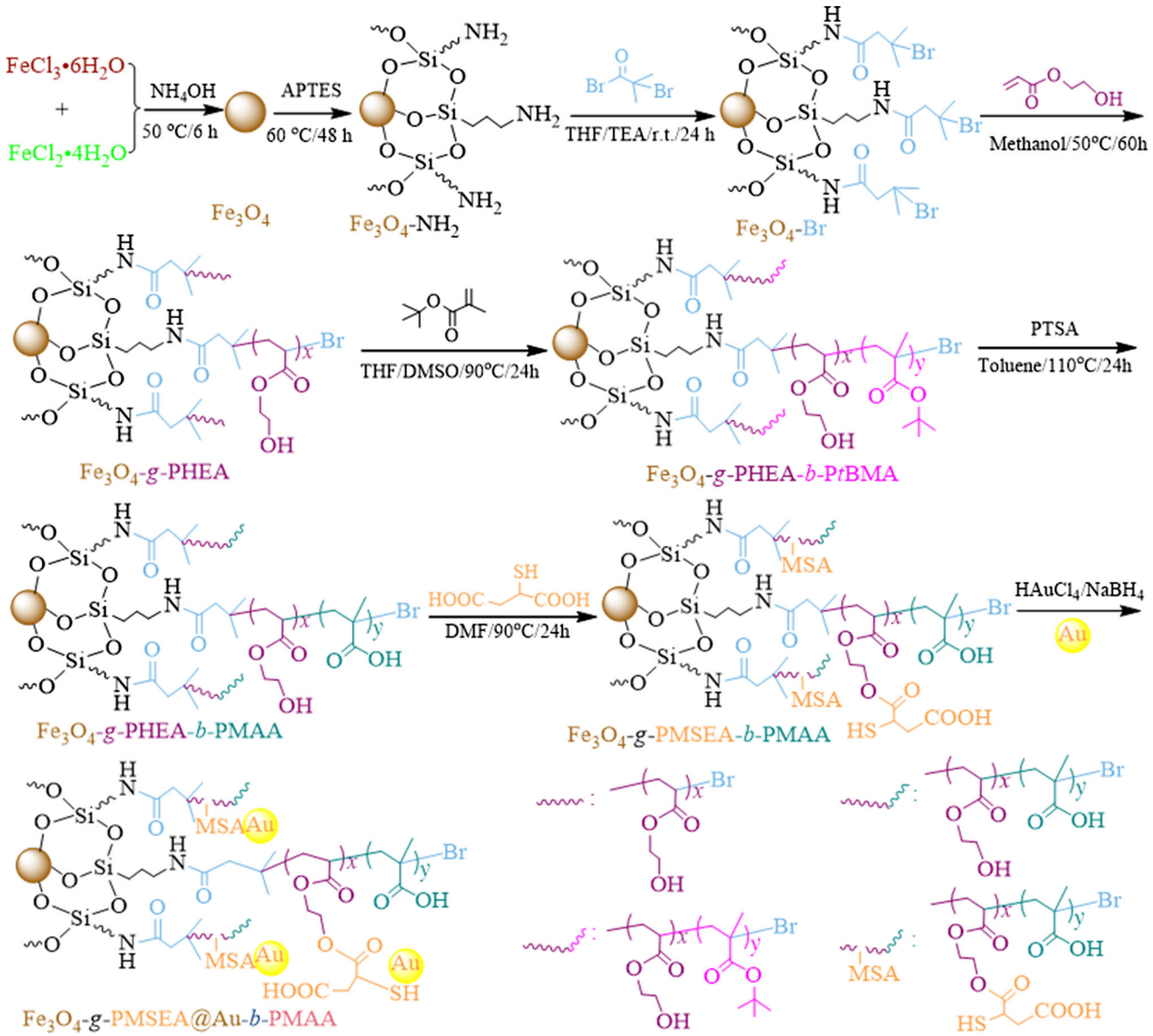

Scheme 1 Synthesis scheme of Fe_3O_4-*g*-PMSEA@Au-*b*-PMAA copolymer nanohybrids.

Preparation of ATRP initiator, Fe_3O_4–Br

Preparation of ATRP initiator on the surface of Fe_3O_4, Fe_3O_4–Br, was achieved via an acylbromination reaction, as reported elsewhere [31]. Specifically, Fe_3O_4–NH_2 NPs (50.0 mg) were ultrasonically dispersed in anhydrous THF (25.0 ml), and then the above solution was shifted in an ice bath and TEA (2.0 ml) was dropwise added the reaction system within 20 min, with strong mechanical agitation. BIB (1.67 ml) dissolved in THF (8.33 ml) was then added with constant pressure funnel within 1 h at 0 °C. The reaction mixture was continuously stirred for 4 h. After the reaction proceeded for 24 h at room temperature, the mixture solution was filtrated. The brown crude product was rinsed with sodium chloride solution, and then washed with deionized water and ethanol alternately several times, and dried in vacuum at 60 °C for 24 h to give an ATRP initiator, Fe_3O_4–Br (mean yield: 85%).

Surface graft polymerization of HEA on Fe_3O_4

The graft polymerization was carried out through ATRP of HEA using Fe_3O_4–Br as an initiator in a molar ratio of Fe_3O_4–Br:HEA:PMDETA:CuBr of

1:100:2:1 [32]. In detail, Fe_3O_4–Br (0.1 g, 0.931 mmol) was dispersed in absolute methanol (20 ml) via ultrasonication for 30 min. Then, HEA (9.77 ml, 93.1 mmol), PMDETA (0.387 ml, 1.862 mmol) and CuBr (0.134 g, 0.931 mmol) were added into the vessel, accompanying with a "freeze-vacuum-thaw" operation thrice to exhaust air and moisture within the system. The reaction vessel was moved into an oil bath of 50 °C and lasted for 60 h, and then quenched with ethanol. The polymerization solution was centrifuged, and the crude product was alternately rinsed with methanol and acetone and dried in vacuum at room temperature till constant weight to afford a surface-grafted product, Fe_3O_4 graft poly(2-hydroxyethyl acrylate) (Fe_3O_4-*g*-PHEA(-Br)) (3.34 g, mean yield: 30%).

Synthesis of Fe_3O_4-g-PHEA-b-PtBMA

To tune the length of the grafted unit, *t*BMA was polymerized through ATRP using Fe_3O_4-*g*-PHEA-Br as a macroinitiator in a molar ratio of Fe_3O_4-*g*-PHEA-Br:*t*BMA:PMDETA:CuBr of 1:150:2:1 and 1:300:2:1, reported elsewhere [32, 33]. Representatively, Fe_3O_4-*g*-PHEA-Br (0.10 g, 0.0278 mmol) was ultrasonically dispersed in a THF-DMSO mixed solvent (5 ml, $v/v = 1/1$). After that, *t*BMA (0.68 ml, 4.1700 mmol), PMDETA (11.60 µl, 0.0556 mmol) and CuBr (3.40 mg, 0.0278 mmol) were blended in the above solution under the protection of nitrogen atmosphere. After the polymerization reaction proceeded in a 90 °C oil bath for 24 h, the graft magnetic block copolymer was separated through centrifugation. The solid crude product was scoured several times with deionized water and methanol, and dried in vacuum at room temperature till constant weight, offering a Fe_3O_4 graft poly(2-hydroxyethyl acrylate-*block*-tert-butyl methacrylate) product with a short *t*BMA repeating unit (0.25 g, mean yield: 25%), named Fe_3O_4-*g*-PHEA-*b*-P*t*BMA-1. The block copolymer nanohybrid with a relatively long *t*BMA unit was prepared in the same way as mentioned above in a molar ratio of Fe_3O_4-*g*-PHEA-(Br):*t*BMA:PMDETA:CuBr of 1:300:2:1 and expressed as Fe_3O_4-*g*-PHEA-*b*-P*t*BMA-2.

Hydrolysis of Fe_3O_4-g-PHEA-b-PtBMA

To obtain a pH-sensitive magnetic block copolymer, Fe_3O_4 graft poly(2-hydroxyethyl acrylate-*block*-methacrylic acid) (Fe_3O_4-*g*-PHEA-*b*-PMAA), hydrolysis of Fe_3O_4-*g*-PHEA-*b*-P*t*BMA was conducted. Fe_3O_4-*g*-PHEA-*b*-PtBMA (75 mg) was ultrasonically dispersed in dried toluene (30 ml), and then PTSA (75 mg) was added. The hydrolysis reaction proceeded at 110 °C for 24 h in the presence of nitrogen atmosphere. After having been separated by external magnetic field, the solid product was washed with ethanol and dried in vacuum at room temperature till constant weight, giving a pH-sensitive magnetic block copolymer Fe_3O_4-*g*-PHEA-*b*-PMAA-1 and Fe_3O_4-*g*-PHEA-*b*-PMAA-2, corresponding to Fe_3O_4-*g*-PHEA-*b*-P*t*BMA-1 and Fe_3O_4-*g*-PHEA-*b*-P*t*BMA-2.

Esterification reaction of Fe_3O_4-g-PHEA-b-PMAA with MSA

Esterification reaction of Fe_3O_4-*g*-PHEA-*b*-PMAA with MSA was carried out as per a mole ratio of –OH/MSA/DMAP/EDC of 1/1.5/1/1.2. Specifically, Fe_3O_4-*g*-PHEA-*b*-PMAA-1 (0.48 g, 0.056 mmol, –OH 1.57 mmol) was dispersed in an anhydrous DCM and DMF mixed solvent (40 ml, $v/v = 1/1$) through ultrasonication for 1 h, and then DMAP (0.19 g, 1.57 mmol) and MSA (0.35 g, 2.36 mmol) were added as a catalyst and reactant in the system, respectively. The reaction flask containing mixed solution was placed in an ice bath for 3 h, and then EDC as water absorbent (0.36 g, 1.88 mmol)-DCM/DMF solution (20 ml) was dropwise added into the reaction system. Esterification reaction proceeded at room temperature for 36 h. The resulting mixed solution was filtrated, washed by deionized water and ethanol for three times, and dried in vacuum at room temperature overnight to obtain a product, Fe_3O_4 graft poly(acryloyloxyethyl 1-mercaptohemisuccinate-*block*-methacrylic acid) (Fe_3O_4-*g*-PMSEA-*b*-PMAA-1). Fe_3O_4-*g*-PMSEA-*b*-PMAA-2 was acquired as per the same process as the above (Table 1).

Assembly of Au NPs in block copolymer nanohybrids

The preparation of Au NPs was performed via an in situ reduction method according to studies reported previously [34]. Simply, deionized water (18.4 ml), $HAuCl_4{\cdot}3H_2O$ aqueous solution (0.5 ml, 0.05 M) and trisodium citrate aqueous solution (0.5 ml, 0.05 M) were uniformity mixed in a conical flask. Then, $NaBH_4$ solution (0.6 ml, 0.1 M) was dropwise added into the above mixture, and the

Table 1 Physicochemical parameters of Fe_3O_4-*g*-PMSEA(@Au)-*b*-PMAA hybrid block copolymer micelles in aqueous solution

Samples	[PHEA–Br]/[MAA]	CMC (mg L^{-1})	D_h (nm)[b]	PDI[b]	ξ (mV)[b]
Fe_3O_4-*g*-PMSEA-*b*-PMAA-1	1:150	45.8	85.9 ± 5.3	0.299 ± 0.005	− 110.62 ± 3.86
Fe_3O_4-*g*-PMSEA-*b*-PMAA-2	1:300	97.4	103.9 ± 6.4	0.285 ± 0.002	− 145.60 ± 1.33
Fe_3O_4-*g*-PMSEA@Au-*b*-PMAA-1[a]	1:150	22.3	127.7 ± 6.9	0.271 ± 0.001	− 72.09 ± 2.20
Fe_3O_4-*g*-PMSEA@Au-*b*-PMAA-2[a]	1:300	45.8	153.6 ± 9.6	0.296 ± 0.002	− 136.06 ± 1.21

[a]The Au content in Fe_3O_4-*g*-PMSEA@Au-*b*-PMAA-1 and Fe_3O_4-*g*-PMSEA@Au-*b*-PMAA-2 are 1%

[b]DLS and ξ data were obtained in the case of the concentration of the copolymer nanohybrids of 250 mg L^{-1}

reduction reaction proceeded at room temperature for 12 h with violent stirring to form a wine-red Au nanosol. Subsequently, Fe_3O_4-*g*-PMSEA-*b*-PMAA (50 mg) was ultrasonically dispersed in 30 ml ethanol for 3 min, and blended in gold nanosol and stirred at room temperature for 24 h. Eventually, an evenly and well-dispersed Au-coated Fe_3O_4 graft block copolymer nanohybrid was obtained by separating the mixture with external magnetic field, washing with water three times and drying in vacuum until constant weight. The nanohybrids with Au contents of about 1% by energy dispersed X-ray (EDX) technique were denominated Fe_3O_4-*g*-PMSEA@Au-*b*-PMAA-1 and Fe_3O_4-*g*-PMSEA@Au-*b*-PMAA-2 according to the aforementioned correspondence, as tabulated in Table 1. The samples with 3% Au NPs were named Fe_3O_4-*g*-PMSEA@Au-*b*-PMAA-1′ and Fe_3O_4-*g*-PMSEA@Au-*b*-PMAA-2′.

Preparation of Fe_3O_4-*g*-PMSEA@Au-*b*-PMAA hybrid copolymer micelles

Dialysis technique was used to prepare hybrid copolymer micelle aggregates. Briefly, Fe_3O_4-*g*-PMSEA@Au-*b*-PMAA (40 mg) was dissolved in 10 ml DMF under vigorous stirring until the solution became opaque. Then, the solution was encased in a dialysis bag (MWCO: 3500 Da) to dialyze against 1000 ml deionized water for 3 days. The deionized water was updated per hour for the first 3 h, and then once per 8 h. The opaque micelle solution was collected for further determination.

Characterization and measurement

Characterization of copolymer nanohybrids

An EQUINX55 Fourier transform infrared spectrometer (FTIR, Bruker, Germany) was adopted to characterize the structure of the copolymer nanohybrids via KBr pellets. The thermal stability of the copolymer nanohybrids was determined by thermal gravimetric analysis (TGA) on a thermal analysis system (TA Corp., New Castle, USA) in the presence of nitrogen atmosphere at a heating rate of 10 °C min^{-1}. The crystallization behavior was examined via X-ray diffraction (XRD) experiments on a X-ray powder diffractometer (D/max-2550, Rigaku Corp., Japan) with Cu Kα (0.1546 nm) radiation at a voltage of 40 kV, a current of 100 mA and a 2θ scan speed of 8.0° min^{-1}. The magnetic properties of pure Fe_3O_4, Fe_3O_4-*g*-PMSEA-*b*-PMAA and Fe_3O_4-*g*-PMSEA@Au-*b*-PMAA were detected on a vibrating sample magnetometer (VSM, 7307, Lake Shore Corp., USA) at room temperature.

Physicochemical characterization

The micellization behavior was investigated by fluorescence spectroscopy on a fluorescence spectrophotometer (FluoroMax-4, Horiba Ltd., France) with pyrene as probe. The concentration of Fe_3O_4-*g*-PMSEA@Au-*b*-PMAA hybrid copolymer micelles ranges from 1×10^{-4} to 5×10^{-1} mg ml^{-1}. Before measurements, a certain volume of acetone solution of pyrene (5×10^{-4} M) was prepared in dim environments, and then the acetone solution of pyrene of 12 μl was added into a 10-ml flask containing the above micelles to make the concentration of pyrene in the system reach to 6×10^{-7} M. To ensure well mixing of pyrene and micelles, the flasks were stirred overnight at room temperature. The determination was carried out at an excitation wavelength of 332 nm, and the emission wavelength ranging from 365 to 550 nm and the slit width for both excitation and emission of 2 nm.

The morphology of the hybrid copolymer micelles was observed with a field-emission transmission

electron microscope (FETEM, Tecnai G2 F20, FEI, USA) at an acceleration voltage 200 kV. Before observation, a drop of micelle solutions was dipped onto carbon-coated copper grids and then dried at room temperature. The surface morphologies were observed with a scanning electron microscope (SEM, Hitachi, Japan). Energy dispersive spectrometer (EDS) attached to SEM was employed to measure elemental composition and content. Before observation, the micelles were dispersed on the silicon slices and dried at room temperature.

The hydrodynamic diameter (D_h), polydispersity index (PDI) of D_h and *zeta* potentials (ξ) of the hybrid copolymer micelles were measured by a dynamic light scattering (DLS, BI-90Plus, USA) with a 15-mW argon ion laser running at 660 nm and a 90° deflection angle at room temperature. 4.0 ml of each sample (250 mg L^{-1}) with different hydrophilic ratios was withdrawn for determination.

pH Responsiveness of the hybrid copolymer micelles was examined by measuring the change of D_h with pH values on the above DLS. The pH transition point (pHTP) of the micelle solution (concentration: 100 mg L^{-1}) was estimated as the intersect point of two tangents of the plots.

UV–Vis absorption spectra were recorded on a UV–Vis spectrophotometer (UV-6100S, Mapada, Shanghai) to examine the absorption spectra of Au nanosols and Au-containing copolymer hybrids in DMF (250 mg L^{-1}).

Electrochemical detection

To study the electrochemical nature of the copolymer hybrids, cyclic voltammetry (CV) measurements were performed on a CHI 660E electrochemical workstation (Shanghai Chenhua Instrument Co., China) using a glassy carbon electrode (GCE) as a working electrode, a saturated calomel electrode as a reference electrode and a platinum wire electrode as a counter electrode in a 1-M H_2SO_4 solution at a scan rate of 50 mV s^{-1}.

Results and discussion

Preparation and characterization of copolymer nanohybrids

FTIR was employed to identify the structure of all the copolymer nanohybrids and the assembly of Au NPs in the copolymers, as presented in Fig. 1A. Fe_3O_4 NPs exhibit a characteristic vibration peak at 580–640 cm^{-1} in Fig. 1A(a), which is ascribed to the stretch mode of Fe–O bonds in bulk Fe_3O_4 [35]. The appearance of a weak peak at 3445 cm^{-1} is due to the existence of –OH groups on the surface of Fe_3O_4 NPs. For Fe_3O_4–NH_2 NPs in Fig. 1A(b), besides the characteristic Fe–O stretch mode, several new characteristic peaks emerge at 1006, 1580, 2926 and 3385–3530 cm^{-1}, which are attributed to the Si–O stretching, –NH_2 bending, –CH_2 stretching and –NH_2 stretching vibration modes, respectively. In IR spectrum of Fe_3O_4–Br in Fig. 1A(c), weak absorption peaks appear at 1050–1100, 1195, 1545, 1644–1740 and 3394–3447 cm^{-1}, which originate from the newly formed C–O and C–N stretch, –NH– bending, ester carbonyl –C=O and –NH– stretching bands, respectively. After ATRP of HEA as shown in Fig. 1A(d), the characteristic absorption peaks at 3337, 2870–2940, 1728, 1600 and 1050–1080 cm^{-1} are attributed to the –OH, C–H, free C=O, strong inter- or/and intramolecular hydrogen bond-interacted C=O and C–O stretching modes in HEA chains, respectively; the stretch mode of Fe–O bonds in Fe_3O_4 remains unchangeable. Fe_3O_4-*g*-PHEA-*b*-P*t*BMA-1 exhibits characteristic vibration bands at 2840–2966, 1720 and 1005–1166 cm^{-1} ascribed to the C–H, free C=O, and C–O stretching vibrations, respectively, as shown in Fig. 1A(e). In particular, the peaks at 1450 and 1370–1385 cm^{-1} are attributable to the asymmetrical deformation vibration (δ_{as}) of –CH_3 groups and the stretching mode of –$C(CH_3)_3$ in P*t*BMA blocks, respectively. In comparison with FTIR spectra of Fe_3O_4-*g*-PHEA, the red shifts of –OH groups at 3425 cm^{-1} and of C=O groups at 1633 cm^{-1} are much likely due to the incorporation of P*t*BMA moieties, leading to weak inter- or/and intramolecular hydrogen bond or complexation interactions. After acidolysis, the characteristic peak at 1370–1385 cm^{-1} disappears, as depicted in Fig. 1A(f). The –$C(CH_3)_3$ groups are translated into the –COOH groups, and thus the hydrogen bond or complexation interactions between the –OH groups in PHEA and the –COOH

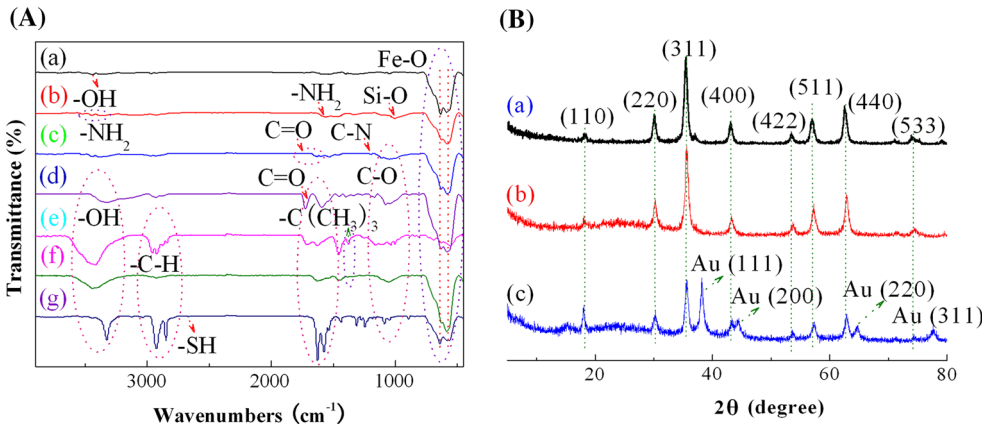

Figure 1 FTIR spectra **A** of (a) Fe_3O_4 NPs, (b) Fe_3O_4–NH_2 NPs, (c) Fe_3O_4–Br, (d) Fe_3O_4-*g*-PHEA, (e) Fe_3O_4-*g*-PHEA-*b*-P*t*BMA-1, (f) Fe_3O_4-*g*-PHEA-*b*-PMAA-1 and (g) Fe_3O_4-*g*-PMSEA-*b*-PMAA-1, and XRD patterns **B** of (a) Fe_3O_4 NPs, (b) Fe_3O_4-*g*-PMSEA-*b*-PMAA-1 and (c) Fe_3O_4-*g*-PMSEA@Au-*b*-PMAA-1.

groups in PMAA moieties are easy enough to generate. No peak attributable to free –OH and –COOH groups emerges, and only a peak reflecting intermacromolecular interactions is located at 1633 cm^{-1}. In addition, the peaks at 3425 and 1054 cm^{-1} are assigned to the –OH and C–O stretch in PHEA and PMAA chains, respectively. For Fe_3O_4-*g*-PMSEA-*b*-PMAA-1 in Fig. 1A(g), a weak vibration peak appears at around 2663 cm^{-1} assigned to the –SH stretching vibration [36]. The bands at 3300 and 1628 cm^{-1} typical of carboxylic groups are shifted slightly to lower wavenumbers, confirming the formation of stronger intermacromolecular interactions between the component polymers. Other vibration bands emerge at 2854–2926 and 1050–1090 cm^{-1} corresponding to the C–H and C–O stretch modes in PMAA and PMSEA blocks, verifying the synthesis of Fe_3O_4-*g*-PMSEA-*b*-PMAA.

XRD was adopted to study the crystal structure of Fe_3O_4 NPs, Fe_3O_4-*g*-PMESA-*b*-PMAA-1 and Fe_3O_4-*g*-PMESA@Au-*b*-PMAA-1, as presented in Fig. 1B. Fe_3O_4 NPs exhibit characteristic diffraction peaks at 18.10°, 30.05°, 35.45°, 43.06°, 53.50°, 57.01°, 62.52° and 73.94°, which are attributed to the (110), (220), (311), (400), (422), (511), (440) and (533) crystal planes of Fe_3O_4 in a cubic phase (JCPDS card No. 85-1436 or PDF#19–0629 and space group: *Fd3m*) [37, 38], respectively. Fe_3O_4-*g*-PMESA-*b*-PMAA produces almost the same diffraction peaks at 18.10°, 30.25°, 35.65°, 43.26°, 53.74°, 57.23° and 62.94° as those of Fe_3O_4 NPs, as shown in Fig. 1B(b). Slight shifts of 2θ angles may be due to the grafting of copolymers on the surface of Fe_3O_4 NPs. In XRD patterns of Fe_3O_4-*g*-PMESA@Au-*b*-PMAA-1 in Fig. 1B(c), in addition to the characteristic peaks of Fe_3O_4 NPs at 18.10°, 30.25°, 35.66°, 43.27°, 53.64°, 57.33° and 62.94°, several new peaks appear at ca. $2\theta = 38.19°$, 44.42°, 64.75° and 77.65°, which are assigned to the (111), (200), (220) and (311) planes of Au NPs in a cubic phase (space group: *Fm3m*), respectively [39]. The average crystal size is estimated using Scherrer formula:

$$D = K\lambda/(\beta \cos\theta) \quad (1)$$

where K is Scherrer constant (0.89), λ is incident X-ray wavelength and equal to ca. 0.15418 nm, β is the peak full-width of half-maximum (rad), and θ is diffraction angel (°). Based on the (311) plane for Fe_3O_4 and the (111) plane for Au NPs coordinated in Fe_3O_4-*g*-PMESA-*b*-PMAA that show strong diffractions, the average crystal size of Fe_3O_4 and Au NPs is calculated to be ca 12.04 and 10.01 nm, respectively.

Figure 2A shows TGA traces of the prepared various samples. Pure Fe_3O_4 NPs in Fig. 2A(a) produce a maximal mass loss of only 6.80% until 800 °C, which is related to the absorbed water (< 175 °C) and the dissociation of –OH groups on their surface (175–475 °C) [40]. In TGA trace of the silanized Fe_3O_4–NH_2 NPs (Fig. 2A(b)), a trace weight loss of 6.8% until around 460 °C may mainly be attributed to the degradation of aminopropyl groups [41]. In Fig. 2A(c), the mass loss of about 13.6% until 800 °C belongs to the decomposition of aminopropyl and bromoisobutyryl groups. The augment of the mass loss is due to the incorporation of bromoisobutyryl groups onto the surface of Fe_3O_4 NPs, suggesting successful preparation of ATRP initiator Fe_3O_4–Br. The thermal degradation of Fe_3O_4-*g*-PHEA is typically divided into two stages, as illustrated in Fig. 2A(d). The mass loss of about 10.1% below 225 °C is attributed to the residues of monomer and solvents, as well as physically absorbed water, etc. With increasing the temperature to 750 °C, the

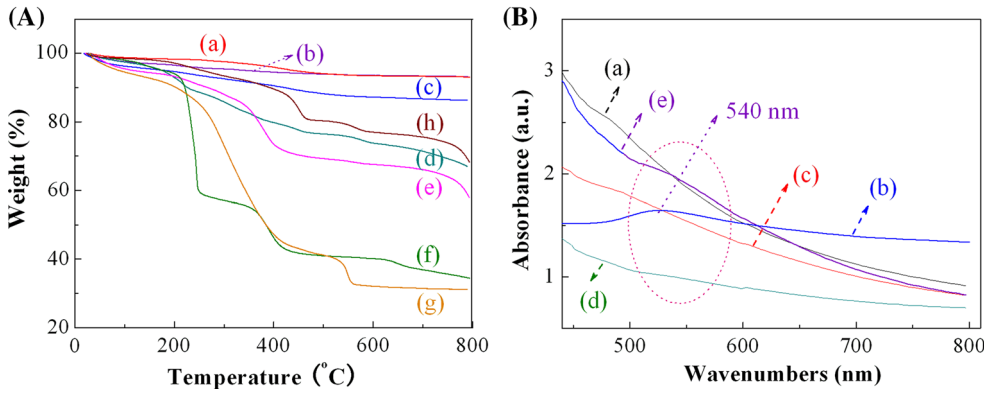

Figure 2 Thermograms **A** of (a) Fe_3O_4 NPs, (b) Fe_3O_4–NH_2 NPs, (c) Fe_3O_4–Br, (d) Fe_3O_4-*g*-PHEA, (e) Fe_3O_4-*g*-PHEA-*b*-P*t*BMA, (f) Fe_3O_4-*g*-PHEA-*b*-PMAA, (g) Fe_3O_4-*g*-PMSEA-*b*-PMAA and (h) Fe_3O_4-*g*-PMSEA@Au-*b*-PMAA, and UV–Vis absorption spectra **B** of (a) Fe_3O_4 NPs, (b) Au NPs (c) Fe_3O_4-*g*-PMESA-*b*-PMAA-1, (d) Fe_3O_4-*g*-PMESA@Au-*b*-PMAA-1 (Au content: 1%) and (e) (Fe_3O_4-*g*-PMESA@Au-*b*-PMAA-1′, Au wt%: 3). The concentration of all samples in ethanol is 10 mg L^{-1}.

cumulative mass loss reaches to ca 29.7%; this is attributed to the decomposition of the side groups and backbones of Fe_3O_4-*g*-PHEA [42]. The grafting percentage of PHEA is calculated to be about 19.6%. When P*t*BMA segments are connected with the precursor Fe_3O_4-*g*-PHEA, the weight loss of P*t*BMA and PHEA fragments up to 750 °C is about 36.5%, as illustrated in Fig. 2A(e). The increased mass loss is the evidence of the incorporation of P*t*BMA blocks. Particularly, the sudden mass decline of curve (e) in Fig. 2A from 350 to 420 °C distinctly differs from the mass loss behavior of Fe_3O_4-*g*-PHEA, which is mainly ascribed to the decomposition of PtBMA backbones [43]. For the hydrolyzed product, Fe_3O_4-*g*-PHEA-*b*-PMAA, three thermal weight loss events can be found in Fig. 2A(f): the removal of residual monomer, solvents and superficial water below 220 °C, dehydration or/and decarboxylation of both intra- and intermolecular carboxyl groups from 220 to 360 °C, and dissociation of the copolymer backbones above 360 °C [44, 45], and the cumulative mass loss accounts for about 6.5, 44.6 and 64.3%, respectively. In Fig. 2A(g), three weight loss stages appear at below 220, 220–520 and above 520 °C, and the mass loss is about 11.5, 59.5 and 69.0%, respectively. The difference in mass loss of 4.7% until 750 °C indicates MSA may be incorporated in Fe_3O_4-*g*-PHEA-*b*-PMAA through esterification reaction with HEA. When Au NPs are anchored on Fe_3O_4-*g*-PMESA-*b*-PMAA as shown in Fig. 2A(h), it is incredible that the maximal weight loss of Fe_3O_4-*g*-PMESA@Au-*b*-PMAA has only 26.3% until 750 °C. Moreover, there is no obvious decarboxylation from 220 to 420 °C, and until 520 °C, the cumulative mass loss is only 19.5%. Above 520 °C, the copolymer backbones start to degrade. The excellent heat stability of the Fe_3O_4-*g*-PMESA@Au-*b*-PMAA over the Fe_3O_4-*g*-PMESA-*b*-PMAA is maybe ascribed to the interaction between Au NPs and the grafted PMESA-*b*-PMAA copolymers including the coordination between Au NPs and –SH groups and the interaction of Au NPs with the –COOH groups of PMAA and PMSEA blocks [46, 47]. In particular, the formation of gold thiolates based on aurophilic interactions accounts for the increased thermal stability [48]. These results suggest that Au NPs are inserted or decorated in the copolymer nanohybrids through a coordination interaction between Au NPs and –SH groups.

Figure 2B depicts UV–Vis absorption spectra of various samples especially containing Au NPs. In Fig. 2B(a), the appearance of low intense hump below 500 nm (ca 480 nm) maybe originates primarily from the absorption and scattering of light by magnetic nanoparticles [49, 50]. Fe_3O_4-*g*-PMESA-*b*-PMAA generates a similar hump, but the intensity is significantly weaker than that produced by Fe_3O_4 NPs because of the grafting of PMESA-*b*-PMAA copolymers, as demonstrated in Fig. 2B(c). However, Au NPs produce a characteristic surface plasmon resonance (SPR) peak at around 520–525 nm, which is strongly dependent upon the size/thickness, shape, interparticle distance, surface coverage and surrounding medium of metal nanoparticles, etc. [51, 52]. In the UV–Vis absorption spectrum of Fe_3O_4-*g*-PMESA@Au-*b*-PMAA copolymer nanohybrids, the absorption band becomes weak and slightly red shifts

to ca. 540 nm. One possible explanation is that the charge transfer exists between Au NPs and –SH groups; the electron deficiency on the surface of Au NPs may lead to the red shift [51]. The plasmon resonance peaks obviously increase with increasing the contents of Au NPs from 1 to 3%, as shown in Fig. 2B(d, e). For these samples decorated with Au NPs, no low intense hump below 500 nm appears due to strong SPR peaks of Au NPs. This signifies that Au NPs are actually incorporated or immobilized in the final block copolymers.

Self-assembly physicochemical properties

Fe_3O_4-*g*-PMESA@Au-*b*-PMAA is a block copolymer hybrid exhibiting amphiphilicity, with pH-sensitive hydrophilic PMAA fragments and hydrophobic Fe_3O_4-*g*-PMESA@Au segments. Consequently, it can spontaneously assemble into a special copolymer micelle in a selected solvent via dialysis technique. To verify the self-assembled micellization process, fluorescence emission spectra of micelle samples with various concentrations were detected, and curves of the fluorescence intensity ratios (I_3/I_1) versus the logarithms of the micelle concentrations can be used to estimate the critical micelle concentration (CMC), as depicted in Fig. S1 of supporting information (SI) and Table 1. Generally, CMC is defined as a polymeric concentration showing a discontinuous change in I_3/I_1 [53]. As expected, Fe_3O_4-*g*-PMSEA-*b*-PMAA-2 has a higher CMC value of about 97.4 mg L^{-1} than Fe_3O_4-*g*-PMSEA-*b*-PMAA-1 (45.8 mg L^{-1}) because the latter has shorter hydrophilic chains than the former, suggesting that the latter possesses a more reasonable hydrophilic/hydrophobic balance and thus is more stable. After Au NPs are coordinated with thiol groups in these copolymer nanohybrids, the CMC value decreases to 45.8 and 22.3 mg L^{-1}, which corresponds to Fe_3O_4-*g*-PMSEA@Au-*b*-PMAA-2 and Fe_3O_4-*g*-PMSEA@Au-*b*-PMAA-1, respectively. The micelles bearing a low CMC value are not prone to dissociating into unimers when they suffer isometric dilution [53]. The decreased CMC values after Au NPs are coordinated may probably be due to aggregation through aurophilic interactions that makes gold thiolates be able to self-associate [48]. The interaction of small Au NPs with the negatively charged –COOH groups of PMAA and PMSEA blocks also brings down the CMC values [47].

Figure 3 exhibits TEM and SEM microphotographs of copolymer micelle nanoparticles formed in aqueous solution. Fe_3O_4 NPs take on homogeneously distributed globular topologies and narrow particle size distribution, with a mean particle size of about 12 nm, as shown in Fig. 3a, which is consistent with that by XRD. After PMSEA-*b*-PMAA is grafted onto the surface of Fe_3O_4 NPs, the hybrid copolymer micelles with core–shell spherical morphologies are formed, with Fe_3O_4 NPs and PMSEA blocks as cores and PMAA blocks as shells, as demonstrated in Fig. 3b, c. The size of the micelles ranges from about 50 to 72 nm and the mean size of about 65 nm for Fe_3O_4-*g*-PMSEA-*b*-PMAA-1, and from 66 to 109 nm and the mean size 85 nm for Fe_3O_4-*g*-PMSEA-*b*-PMAA-2. Clearly, the average thickness of the copolymer layers of about 53 nm for Fe_3O_4-*g*-PMSEA-*b*-PMAA-1 and about 73 nm for Fe_3O_4-*g*-PMSEA-*b*-PMAA-2 surround the Fe_3O_4 NPs in the hybrid copolymer micelles. In addition, the density of Fe_3O_4-*g*-PMSEA-*b*-PMAA is measured by a pycnometer to be about 1.21 g cm^{-3}, lower than that of pure Fe_3O_4 NPs of 1.79 g cm^{-3} due to the surface graft of PMSEA-*b*-PMAA that has low density. It is therefore inferred that quite a lot of PMSEA-*b*-PMAA has been anchored on the surface of Fe_3O_4 NPs, which makes for better dispersion stability, and can prevent sedimentation and agglomeration of Fe_3O_4 NPs [39]. DLS determination indicates that the hybrid copolymer nanomicelles in aqueous solution possess hydrodynamic diameters (D_h) centered at about 85.9 nm for Fe_3O_4-*g*-PMSEA-*b*-PMAA-1 and 103.9 nm for Fe_3O_4-*g*-PMSEA-*b*-PMAA-2, as shown in Fig. S2(a) and (b) of SI and Table 1. The values are higher than those estimated by TEM because the grafted amphiphilic block copolymers are in a swelling state during DLS determination, whereas they are in a contraction state upon observed with TEM. The hybrid copolymer nanomicelles possess narrow size distribution, with polydispersity index (PDI) of particle sizes below 0.3. With increasing the feed ratios of MAA or the length of PMAA blocks, the D_h values increase because of longer hydrophilic shell layers. SEM observation corroborates the spherical morphologies formed by the copolymer nanohybrid in aqueous solution, and the particle size ranges from about 80 to 155 nm, as shown in Fig. 3d. The inset in Fig. 3d gives clearer smooth globular core–shell micellar topology, and the micellar size is about 155 nm. Nevertheless, the copolymer hybrid

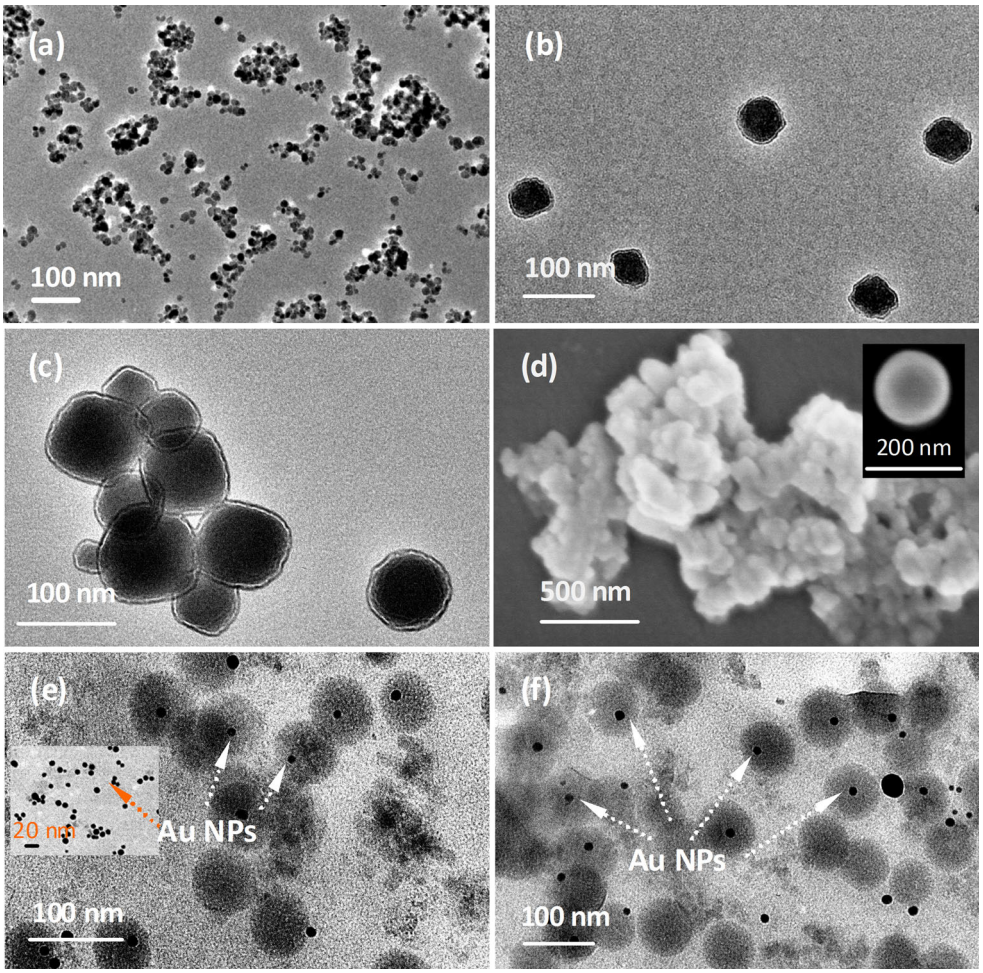

Figure 3 TEM photographs of **a** Fe_3O_4 NPs, **b** Fe_3O_4-*g*-PMSEA-*b*-PMAA-1, **c** Fe_3O_4-*g*-PMSEA-*b*-PMAA-2, **e** Fe_3O_4-*g*-PMSEA@Au-*b*-PMAA-1 and **f** Fe_3O_4-*g*-PMSEA@Au-*b*-PMAA-2 (the inset shows TEM microphotographs of Au NPs), and **d** SEM image of Fe_3O_4-*g*-PMSEA-*b*-PMAA-2 (Au contents in all the copolymer hybrids are 1 wt%; the copolymer hybrid has a concentration of 500 mg L^{-1} in aqueous solution).

nanomicelles in Fig. 3d are gathered together probably due to high concentrations of the copolymer hybrids.

Au NPs present uniform globular morphologies, and the particle size ranges from 6 to 15 nm, and the average size is about 11 nm, as depicted in insets of Fig. 3e. The copolymer nanohybrids combined with Au NPs give "waxberry-like" globular topologies as shown in Fig. 3e, f; this may be incorporation of Au NPs in the side chains of the grafted block copolymers on the surface of Fe_3O_4 NPs through complexation. The scattered spots on the surface of the "waxberry-like" globular micelles in Fig. 3f have a size of approximately 12 nm, which is consistent with that of Au NPs. Fe_3O_4-*g*-PMSEA@Au-*b*-PMAA-1 and Fe_3O_4-*g*-PMSEA@Au-*b*-PMAA-2 nanomicelles possess a mean TEM size of about 70 and 85 nm, respectively, slightly higher than that before Au NPs are coordinated. The D_h values in Fig. S2(c) and S2(d) of SI and Table 1 give similar results, which further reveal the increased micelle sizes in comparison with the copolymer micelles without Au NPs. To verify the anchoring of Au NPs on the copolymer hybrids, the element overlay and energy dispersed X-ray (EDX) spectra of Fe_3O_4-*g*-PMSEA@Au-*b*-PMAA are collected, as illustrated in Fig. S3 in SI. It is easy to get the information of carbon, nitrogen, oxygen, sulfur, iron, gold and bromine elements, where Fe and N are mainly attributed to the modified Fe_3O_4 NPs, and C and O are predominately assigned to PMSEA and PMAA segments. In particular, the presence of S and Au corroborates the coordination interaction between Au NPs and –SH groups. The mass contents of these elements are separately 11, 73, 10, 4, 1 and 1 wt% in sequence of N, O, S, Fe, Au and Br excluding C, and the mass of Au is reasonably lower than that of S. These findings disclose the successful preparation of the block copolymer nanohybrids.

Zeta potential (ξ) is an important index reflecting the stability of colloidal dispersions. Considering the possible applications of the present work in biomedical areas, the stability of the self-assembly micelles is important for effective drug release [54, 55]. Generally, stable assemblies can minimize the drug release at normal cells and thus maximally avoid the harm to normal cells or tissues. Therefore, *zeta* potentials of the resulting copolymer hybrids are determined in the present work, and summarized in Table 1. Clearly, the absolute values of ξ of the copolymer hybrids are significantly high (the absolute values are more than 72 mV) whether they contain Au NPs or not. As a consequence, the copolymer hybrids have apodeictic stability in aqueous environments, which is a crucial factor for drug delivery carriers [56, 57]. The considerably high ξ values may be ascribed to the scattering of a large number of –COOH groups on a nanoscaled micelle surface with large specific area containing Fe_3O_4, making the $–COO^-$ negative charges fully contained within the region bounded by the slipping plane in an electrical double layer. The increase in the absolute values of ξ with increasing the feed ratios of the PMAA length is obviously correlated with more –COOH groups. After Fe_3O_4-*g*-PMSEA-*b*-PMAA copolymers are coordinated with Au NPs; however, ξ values reduce at a certain degree, which may be due to the intense screening effect of Au NPs in the hybrid copolymer micelles, limiting exposure of carboxyl groups.

pH-, magnetic and electrochemical responsiveness

Unique architecture and chemical compositions of Fe_3O_4-*g*-PMSEA-*b*-PMAA and Fe_3O_4-*g*-PMSEA@Au-*b*-PMAA endow them with pH, magnetic and electrochemical responsiveness. pH Response of representative Fe_3O_4-*g*-PMSEA-*b*-PMAA-2 is testified by the change in D_h with pH, as demonstrated in Fig. 4A. Below pH of ca. 5.2, less than the pKa of 5.5–5.6 of PMAA [58], protonated PMAA segments are highly intertwined due to inter- and intramolecular hydrogen bond interactions, lead to the formation of large micelle aggregates. As pH exceeds 5.2, the associated PMAA shell layers start to change from hydrophobicity to hydrophilicity, and large aggregates are disassociated, D_h decreases abruptly. With increasing pH up to about 5.6, the hydrogen bond interactions almost disappear on account of ionization of most of the carboxylic groups. When pH is further increased to 6.1, PMAA shell layers are thoroughly ionized, large micelle aggregates are dissociated into small micelles or unimers, and thus D_h remains almost unchangeable. The pH value at which half of the total decrease in D_h occur is defined as the pH phase transition points (pHTP). As such, the pHTP value of representative Fe_3O_4-*g*-PMSEA-*b*-PMAA-2 is estimated to be about 5.6, equivalent to the p*K*a of PMAA moieties. Likewise, Fe_3O_4-*g*-PMSEA-*b*-PMAA-1 also exhibits pH responsivity at pH of ca 5.5, slightly lower that of the above micelle (Fig. S4 of SI). The pHTP values for Fe_3O_4-*g*-PMSEA@Au-*b*-PMAA-1 and Fe_3O_4-*g*-PMSEA@Au-*b*-PMAA-2 slightly shift to about 5.3 and 5.9, respectively, deviating from the p*K*a of PMAA of about ± 0.3 (Fig. S4 of SI). The decreased pHTP for Fe_3O_4-*g*-PMSEA@Au-*b*-PMAA-1 is ascribed to the incorporation of Au NPs, which more easily leads to aggregation of the nanomicelles through aurophilic in addition to hydrogen bond interactions at acidic media, whereas at (alkalescence) environments in the vicinity of p*K*a, the aggregated nanomicelles are promptly disassociated and the interaction of Au NPs with $–COO^-$ anions weakens or/and disappears. Slight increase of pHTP for Fe_3O_4-*g*-PMSEA-*b*-PMAA-2 and Fe_3O_4-*g*-PMSEA@Au-*b*-PMAA-2 with increasing the length of PMAA chains is due to slower disassociation of the aggregated nanomicelles with more interactions described above. It follows that the copolymer nanohybrids exhibit pH responsive property that can be properly tailored, as expected, which provides a choice of drug controlled release.

To investigate the electrochemical properties of the prepared nanohybrids, cyclic voltammetry (CV) curves were detected, as shown in Fig. 4B (fine CV curves for samples a–c and e are demonstrated in Fig. S5 of SI). The glass carbon electrodes modified with Fe_3O_4 NPs produce the anodic and cathodic peak currents at a potential of 1.52 and − 0.22 V, respectively, due to its conductivity [59–61]. However, for Fe_3O_4-*g*-PMSEA-*b*-PMAA-2 in Fig. 4B(b), hardly any oxidation and reduction peak is observed in that the graft of PMSEA-*b*-PMAA restricts the exposure of Fe_3O_4 NPs in the electrolytes and reduces the rate of electron transfer [49]. The PMSEA-*b*-PMAA layer therefore plays the role of a barrier hindering the electron transfer on the surface of Fe_3O_4 NPs and is not a suitable candidate as electron

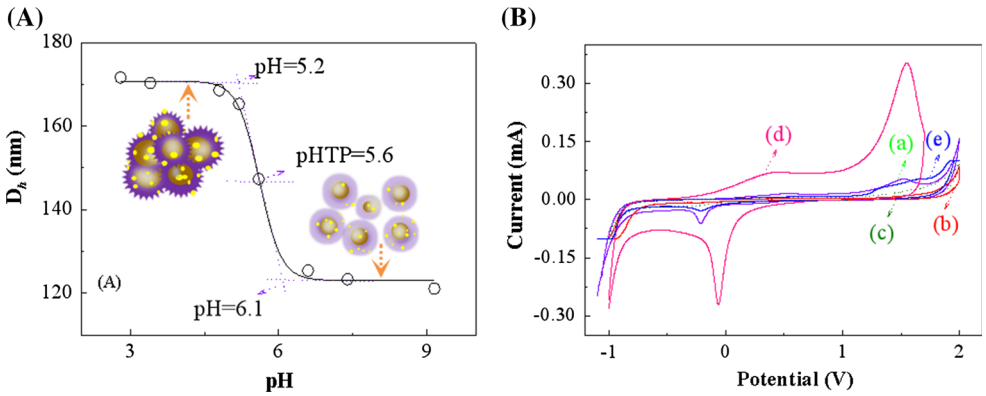

Figure 4 **A** pH sensitivity of representative Fe_3O_4-*g*-PMSEA-*b*-PMAA-2 (concentration: 100 mg L^{-1}) revealed by the plot of D_h versus pH, and **B** CV curves of (a) bare Fe_3O_4 NPs, (b) Fe_3O_4-*g*-PMSEA-*b*-PMAA-2, (c) Fe_3O_4-*g*-PMSEA@Au-*b*-PMAA-2′ (Au wt%: 3), (d) Fe_3O_4-*g*-PMSEA@Au-*b*-PMAA-1′ (Au wt%: 3) and (e) Fe_3O_4-*g*-PMSEA@Au-*b*-PMAA-1 (Au wt%: 1) at a scan rate 0.1 V s^{-1}. The concentration of all the samples in methanol is 100 mg L^{-1}.

carriers [60, 61]. After Au NPs are conjugated with Fe_3O_4-*g*-PMSEA-*b*-PMAA-2 in Fig. 4B(c), a weak reduction peak can be observed due to the coordination of Au NPs that possess excellent electrochemical properties. Decreasing the length of the grafted PMSEA-*b*-PMAA block chains for the same content of Au NPs leads to the large increment of the oxidation and reduction peak currents, which locates at 390 and − 58 mV, respectively, as shown in Fig. 4B(d). This indicates that the short PMSEA-*b*-PMAA chains make for electron transfer, and thus show the strong redox capacity [34]. The Au content in Fe_3O_4-*g*-PMSEA@Au-*b*-PMAA-1 has influence on electrochemical properties, as shown in Fig. 4B(e). For the copolymer nanohybrid containing the Au content 1 wt%, the anodic and cathodic peak currents obviously decrease at 1.34 and − 0.22 V, respectively, and the peak separation at anode and cathode ($\Delta E = E_a - E_c$) is enhanced. Generally, the peak separation of cathode and anode would affect the reversibility of the electrochemical response, and a decreased ΔE value hints increased redox reversibility [62]. In comparison with any other modified electrodes having a ΔE value of about 1.75 V, the nanohybrid-modified electrode with a short PMAA graft chain and relatively high Au loading gives a small ΔE value of about 0.39 V, thus offering improved reversibility of the electrochemical response. Therefore, it is concluded that the reversibility of the electrochemical response can be improved by tuning the length of the PMAA graft chains and the loading percentage of Au NPs. To obtain an optimal modified electrode material, more effort is needed to achieve an optimal balance between the loading percentage of Au NPs, the length of the graft chains and the electrochemical properties of the copolymer nanohybrids.

Figure 5A shows hysteresis loops of the prepared copolymer nanohybrids at 300 K by VSM measurements. It is noticed that the saturation magnetization (M_s) is 58.26, 40.45 and 42.36 emu g^{-1} for Fe_3O_4 NPs, Fe_3O_4-*g*-PMSEA-*b*-PMAA-2 and Fe_3O_4-*g*-PMSEA@Au-*b*-PMAA-2, respectively. These data suggest that the prepared copolymer nanohybrids possess ferromagnetism. The obvious decrease of M_s for the copolymer nanohybrids in comparison with Fe_3O_4 NPs is attributable to the incorporation of PMSEA-*b*-PMAA copolymers with no magnetism on the surface of Fe_3O_4 NPs. In comparison, the conjugation of Au NPs in Fe_3O_4-*g*-PMSEA-*b*-PMAA leads to a slight increase of M_s; this is probably because the strong Au–S covalent interaction leads to the transfer of 5*d* electrons in Au atoms into S atoms, which causes local 5*d* electron-holes (or emergence of unpaired electrons) and the follow-up spin polarization, and thus induces certain ferromagnetism or magnetic properties [63, 64]. It is just the unique magnetism of Au NPs that results in the overlapping of the magnetism of Fe_3O_4-*g*-PMSEA-*b*-PMAA copolymer nanohybrids, thus enhancing the saturation magnetization M_s of the resulting copolymer hybrids and altering the magnetic behavior of Fe_3O_4-*g*-PMESA-*b*-PMAA. Therefore, it is clear that the magnetism of the resulting copolymer hybrids is mainly contributed by Fe_3O_4 NPs plus the effect of Au NPs. In consideration of the surface plasma resonance, pH sensitivity and electrochemical properties, the Fe_3O_4-*g*-PMSEA@Au-*b*-

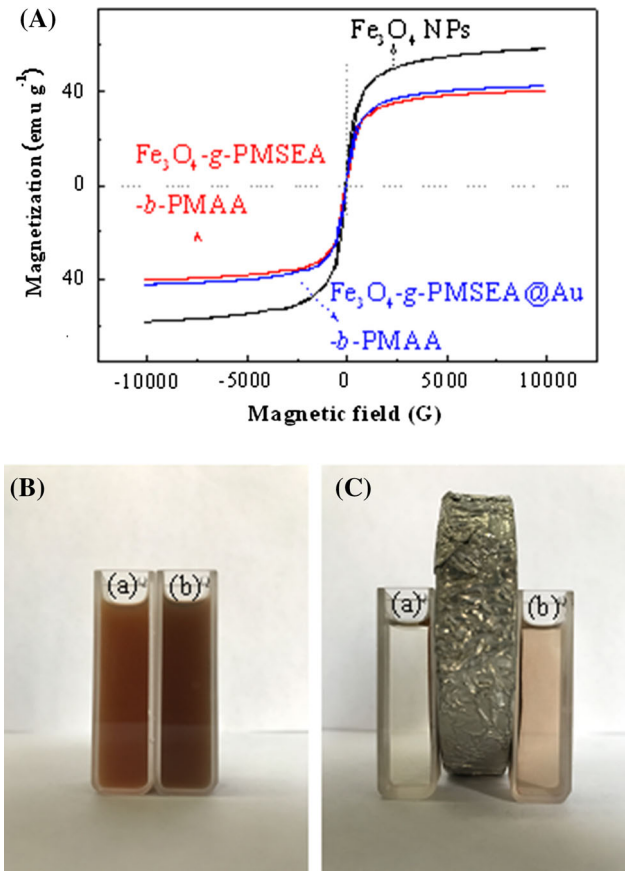

Figure 5 **A** Magnetization curves of Fe_3O_4 NPs, Fe_3O_4-*g*-PMSEA-*b*-PMAA-1 and Fe_3O_4-*g*-PMSEA@Au-*b*-PMAA-1 (Au content: 1 wt%), and **B**, **C** digital photographs of (a) Fe_3O_4-*g*-PMSEA-*b*-PMAA and (b) Fe_3O_4-*g*-PMSEA@Au-*b*-PMAA: **B** in absence of and **C** in the presence of applied magnetic field. The concentration of all samples is 10 mg L^{-1}.

PMAA copolymer nanohybrids are preferable in this study. Since many factors including the coating agents, and the size and distribution of Au NPs affect the magnetism of Au NPs, there is still much work to do to make certain the magnetic mechanism of Au NPs [65]. When the external magnetic field is removed, the copolymer nanohybrids almost lose their magnetism, with negligible coercive forces (H_c) and remanent magnetization (M_r), as summarized in Table S1 in SI. It is clear that Fe_3O_4-*g*-PMSEA-*b*-PMAA-2 and Fe_3O_4-*g*-PMSEA@Au-*b*-PMAA-2 possess H_c values less than 33.3 and 37.6 G, and M_r values smaller than 2.3 and 2.3 emu g^{-1}, respectively. These findings disclose that the copolymer nanohybrids are superparamagnetic and exhibit characteristics of soft magnetic materials [66]. They can be easily magnetized and demagnetized, and when the magnetic field is exerted, they can regain magnetism. The magnetic properties are anticipated to be potentially applied in the areas of magnetically targeted therapy.

This trait of the block copolymer nanohybrids can make them be separated from the reaction medium rapidly and easily in a magnetic field, and also be well dispersed by gentle shaking when the external magnetic field is removed. As shown in Fig. 5B, under no external magnetic field, Fe_3O_4-*g*-PMSEA-*b*-PMAA and Fe_3O_4-*g*-PMSEA@Au-*b*-PMAA form uniform light brown and nigger brown solution in dichloromethane through ultrasonication, respectively. When a magnet is placed next to the solution, the copolymer nanohybrids are attracted to the side walls of cuvettes where the magnet stands, leaving pellucid solution, as demonstrated in Fig. 5C. When the magnet is removed, however, the copolymer nanohybrids are redispersed and form homogenous solution. These phenomena indicate that the block copolymer nanohybrids have been endowed with the magnetic responsibility.

Conclusion

In summary, well-defined Au NPs coordinated Fe_3O_4 graft block copolymer nanohybrids were synthesized via surface-initiated ATRP, and the follow-up esterification of MSA and complexation, as confirmed by FTIR, XRD, TGA, UV–Vis, EDX and density measurements, etc. The block copolymer nanohybrids could spontaneously assemble and form globular core–shell copolymer micelles in aqueous solution. The size, CMC and *zeta* potentials of the micelles vary with compositional proportions of each fragment and the coordination of Au NPs. The block copolymer nanohybrids exhibited multifunctionality of pH, electrochemical, plasmon resonance and magnetic stimuli responsiveness. By adjusting the chemical compositions of the copolymer hybrids, the physicochemical parameters and properties including pHTP, CMC, *zeta* potentials, micelle size and magnetism, and photoelectrical properties such as UV–Vis absorption and electrochemical properties could be modulated accordingly. In the future, the wide applications of the multifunctional nanohybrids in many fields will be investigated to fully play and gain their values.

Acknowledgements

This work is supported by the Fundamental Research Funds for the Central Universities (2016TS049 and GK201601003).

Electronic supplementary material: The online version of this article (doi:10.1007/s10853-017-1675-4) contains supplementary material, which is available to authorized users.

References

[1] Hoheisel TN, Hur K, Wiesner UB (2015) Block copolymer-nanoparticle hybrid self-assembly. Prog Polym Sci 40:3–32

[2] Chen Y, Du J, Xiong M, Zhang K, Zhu H (2006) Gelation inside block copolymer aggregates and organic/inorganic nanohybrids. Macromol Rapid Commun 27:741–750

[3] Schumacher M, Ruppel M, Yuan J, Schmalz H, Colombani O, Drechsler M, Müller AHE (2009) Smart organic–inorganic nanohybrids based on amphiphilic block copolymer micelles and functional silsesquioxane nanoparticles. Langmuir 25:3407–3417

[4] Pang H, Xu L, Yan DX, Li ZM (2014) Conductive polymer composites with segregated structures. Prog Polym Sci 39:1908–1933

[5] Zhang J, Luo YL, Xu F, Chen YS (2016) Novel poly(*N*-vinylcarbazole) grafted multi-walled carbon nanotube nanocomposites based on a nucleophilic reaction: synthesis, fabrication of thin films, and sensing properties. Chem Eng J 298:136–145

[6] Cobley CM, Chen J, Cho EC, Wang LV, Xia Y (2010) Gold nanostructures: a class of multifunctional materials for biomedical applications. Chem Soc Rev 40:44–56

[7] Whittell GR, Manners I (2010) Metallopolymers: new multifunctional materials. Adv Mater 19:3439–3468

[8] Nicole L, Rozes L, Sanchez C (2010) Integrative approaches to hybrid multifunctional materials: from multidisciplinary research to applied technologies. Adv Mater 22:3208–3214

[9] Wang J, Sun X, Mao W, Sun W, Tang J, Sui M, Shen Y, Gu Z (2013) Tumor redox heterogeneity-responsive prodrug nanocapsules for cancer chemotherapy. Adv Mater 25:3670–3676

[10] Hu YW, Du YZ, Liu N, Liu X, Meng TT, Cheng BL, He JB, You J, Yuan H, Hu FQ (2015) Selective redox-responsive drug release in tumor cells mediated by chitosan based glycolipid-like nanocarrier. J Control Release 206:91–100

[11] Xu JW, Gao ZD, Han K, Liu Y, Song YY (2014) Synthesis of magnetically separable $Ag_3PO_4/TiO_2/Fe_3O_4$ heterostructure with enhanced photocatalytic performance under visible light for photoinactivation of bacteria. ACS Appl Mater Inter 6:15122–15131

[12] Challagulla S, Nagarjuna R, Ganesan R, Roy S (2016) Acrylate-based polymerizable sol-gel synthesis of magnetically recoverable TiO_2 supported Fe_3O_4 for Cr(VI) photoreduction in aerobic atmosphere. ACS Sustain Chem Eng 4:974–982

[13] Bao J, Chen W, Liu T, Zhu Y, Jin P, Wang L, Liu J, Wei Y, Li Y (2007) Bifunctional Au–Fe_3O_4 nanoparticles for protein separation. ACS Nano 1:293–298

[14] Sun S, Murray CB, Weller D, Folks L, Moser A (2000) Monodisperse FePt nanoparticles and Ferromagnetic FePt nanocrystal superlattices. Science 287:1989–1992

[15] Cheng K, Peng S, Xu C, Sun S (2009) Porous hollow Fe_3O_4 nanoparticles for targeted delivery and controlled release of cisplatin. J Am Chem Soc 131:10637–10644

[16] Bao Y, Wen T, Samia ACS, Khandhar A, Krishnan KM (2016) Magnetic nanoparticles: material engineering and emerging applications in lithography and biomedicine. J Mater Sci 51:513–553. doi:10.1007/s10853-015-9324-2

[17] Xu C, Ouyang C, Jia R, Li Y, Wang X (2009) Magnetic and optical properties of poly(vinylidene difluoride)/Fe_3O_4 nanocomposite prepared by coprecipitation approach. J Appl Polym Sci 111:1763–1768

[18] Terzi F, Zanfrognini B, Zanardi C, Pigani L, Seeber R (2011) Poly(3,4-ethylenedioxythiophene)/Au-nanoparticles composite as electrode coating suitable for electrocatalytic oxidation. Electrochim Acta 56:3575–3579

[19] Sebez B, Su L, Ogorevc B, Tong Y, Zhang X (2012) Aligned carbon nanotube modified carbon fiber coated with gold nanoparticles embedded in a polymer film: voltammetric microprobe for enzymeless glucose sensing. Electrochem Commun 25:94–97

[20] Balalakshmi C, Gopinath K, Govindarajan M, Lokesh R, Arumugam A, Alharbi NS, Kadaikunnan S, Khaled JM, Benelli G (2017) Green synthesis of gold nanoparticles using a cheap Sphaeranthus indicus extract: impact on plant cells and the aquatic crustacean Artemia nauplii. J Photochem Photobiol B Biol 173:598–605

[21] Kumar A, Boruah BM, Liang XJ (2011) Gold nanoparticles: promising nanomaterials for the diagnosis of cancer and HIV/AIDS. J Nanomater 2011:202187

[22] Xu C, Ho D, Xie J, Wang C, Kohler N, Walsh EG, Morgan JR, Chin YE, Sun S (2008) Au–Fe_3O_4 dumbbell nanoparticles as dual-functional probes. Angew Chem Int Ed Engl 47:173–176

[23] Xu X, Song L, Zheng Q, Cao X, Yao C (2017) General preparation of heme protein functional Fe_3O_4@Au-Nps magnetic nanocomposite for sensitive detection of hydrogen peroxide. Electroanalysis 29:765–772

[24] Wu Y, Yang H, Lin Y, Zheng Z, Ding X (2016) Poly(*N*-isopropylacrylamide) modified Fe_3O_4@Au nanoparticles with magnetic and temperature responsive properties. Mater Lett 169:218–222

[25] Ma Y, Liang X, Tong S, Bao G, Ren Q, Dai Z (2013) Gold nanoshell nanomicelles for potential magnetic resonance imaging, light-triggered drug release, and photothermal therapy. Adv Funct Mater 23:815–822

[26] Wang T, Petrenko VA, Torchilin VP (2010) Paclitaxel-loaded polymeric micelles modified with MCF-7 cell-specific phage protein: enhanced binding to target cancer cells and increased cytotoxicity. Mol Pharm 7:1007–1014

[27] Qiu L, Qiao M, Chen Q, Tian C, Long M, Wang M, Li Z, Hu W, Li G, Cheng L, Cheng L, Hu H, Zhao X, Chen D (2014) Enhanced effect of pH-sensitive mixed copolymer micelles for overcoming multidrug resistance of doxorubicin. Biomaterials 35:9877–9887

[28] Patil SS, Wadgaonkar PP (2017) Temperature and pH dual stimuli responsive PCL-*b*-PNIPAAm block copolymer assemblies and the cargo release studies. J Polym Sci, Part A: Polym Chem 55:1383–1396

[29] Di H (2012) Fabrication and performance of P(MAA-*co*-AAm)/Fe_3O_4 as polymer magnetic composites. J Nat Sci Heilongjiang Univ 29:797–803

[30] Hu W, Lou ZW (2013) Amination surface-modification of ferriferous oxide magnetic nanoparticles. Chem Res (in Chinese) 2:144–148

[31] Wang Y, Zhang Y, Hou C, He X, Liu M (2016) Preparation of a novel TETA functionalized magnetic PGMA nano-absorbent by ATRP method and used for highly effective adsorption of Hg(II). J Taiwan Inst Chem Eng 58:283–289

[32] Liu J, Feng N, Chang S, Kang H (2012) Preparation and characterization of poly(glycidyl methacrylate) grafted from magnesium hydroxide particles via SI-ATRP. Appl Surf Sci 258:6127–6135

[33] Wu H, Tang L, An L, Wang X, Zhang H, Shi J, Yang S (2012) PH-responsive magnetic mesoporous silica nanospheres for magnetic resonance imaging and drug delivery. React Funct Polym 72:329–336

[34] Choi HJ, Jeon IY, Chang DW, Yu D, Dai L, Tan LS, Baek JB (2011) Preparation and electrocatalytic activity of gold nanoparticles immobilized on the surface of 4-mercaptobenzoyl-functionalized multiwalled carbon nanotubes. J Phys Chem C 115:1746–1751

[35] Tarasi R, Khoobi M, Niknejad H, Ramazani A, Mamani L, Bahadorikhalili S, Shafiee A (2016) β-cyclodextrin functionalized poly (5-amidoisophthalicacid) grafted Fe_3O_4 magnetic nanoparticles: a novel biocompatible nanocomposite for targeted docetaxel delivery. J Magn Magn Mater 417:451–459

[36] Hazra S, Joshi H, Ghost BK, Ahmed A, Gibson T, Millner P, Ghosh NN (2015) Development of a novel and efficient H_2O_2 sensor by simple modification of a screen printed Au electrode with Ru nanoparticle loaded functionalized mesoporous SBA15. RSC Adv 5:34390–34397

[37] Han Y, Lei S, Lu J, He Y, Chen Z, Ren L, Zhou X (2016) Potential use of SERS-assisted theranostic strategy based on Fe_3O_4/Au cluster/shell nanocomposites for bio-detection, MRI, and magnetic hyperthermia. Mater Sci Eng, C 64:199–207

[38] Wu W, Wu ZH, Yu TY, Jiang CZ, Kim WS (2015) Recent progress on magnetic iron oxide nanoparticles: synthesis, surface functional strategies and biomedical applications. Sci Technol Adv Mater 16:23501–23543

[39] Lo CK, Xiao D, Choi MMF (2007) Homocysteine-protected gold-coated magnetic nanoparticles: synthesis and characterization. J Mater Chem 17:2418–2427

[40] Barandiaran I, Cappelletti A, Strumia M, Eceiza A, Kortaberria G (2014) Generation of nanocomposites based on (PMMA-*b*-PCL)-grafted Fe_2O_3 nanoparticles and PS-*b*-PCL block copolymer. Eur Polym J 58:226–232

[41] Cosio-Castañeda C, Martínez-García R, Socolovsky LM (2014) Synthesis of silanized maghemite nanoparticles onto reduced grapheme sheets composites. Solid State Sci 30:17–20

[42] Asano A, Kurotu T (2002) Thermal stability of the poly(2-hydroxyethyl methacrylate)/poly(methacrylic acid) blend by the intermolecular bond between PHEMA and PMAA and its mobility investigated by 2D WISE NMR. Polym Degrad Stabil 78:137–141

[43] Zhang BZ (2009) Study on dispersion and location of polymer-grafted carbon nanotubes in polymer nanocomposite. Master thesis, Zhejiang University

[44] Xu JW, Xu F, Luo YL (2015) Core crosslinked H-type poly(methacrylic acid)-*block*-hydroxyl terminated polybutadiene-*block*-poly(methacrylic acid) four armed star block copolymer micelles for intercellular drug release. J Bioact Compat Pol 30:349–365

[45] Clausen DN, Pires LMR, Tarley CRT (2014) Improved selective cholesterol adsorption by molecularly imprinted poly(methacrylic acid)/silica(PMAA-SiO_2) hybrid material synthesized with different molar ratios. Mater Sci Eng, C 44:99–108

[46] Wang S, Zhang J, Yuan P, Sun Q, Jia Y, Yan W, Chen Z, Xu Q (2015) Au nanoparticle decorated N-containing polymer spheres: additive-free synthesis and remarkable catalytic

behavior for reduction of 4-nitrophenol. J Mater Sci 50:1323–1332. doi:10.1007/s10853-014-8692-3

[47] Salem JK, El-Nahhal IM, Najri BA, Hammad TM, Kodeh F (2016) Effect of anionic surfactants on the surface plasmon resonance band of silver nanoparticles: determination of critical micelle concentration. J Mol Liq 223:771–774

[48] Yue CY, Chen WD, Jiang FL, Feng R, Hong MC (2013) Two isomeric Au complexes of S-trithiane: one-dimensional polymer assembled through aurophilic interactions. Inorg Chem Commun 13:105–108

[49] Shen W, Shi MM, Wang M, Chen H (2010) A simple synthesis of Fe_3O_4 nanoclusters and their electromagnetic nanocomposites with polyaniline. Mater Chem Phys 122:588–594

[50] Ding YL, Liu FT, Cheng CB, Lin XZ (2012) Co-precipitation synthesis of monodisperse Fe_3O_4 nanoparticles based on modulation of hydrochloric acid. J Synth Cryst 41:468–473

[51] Wei Y, Klajn R, Pinchuk AO, Grzbowski BA (2008) Synthesis, sharp control, and optical properties of hybrid Au/Fe_3O_4 "nanoflowers". Small 4:1635–1639

[52] Sheng Y, Xue J (2012) Synthesis and properties of Au–Fe_3O_4 heterostructured nanoparticles. J Colloid Interf Sci 374:96–101

[53] Luo YL, Huang RJ, Zhang LL, Xu F, Chen YS (2013) Dual-responsive polyacrylate copolymer micelles with PMAA and PNIPAAm graft brushes: physicochemical properties and prednisone release. Colloids Surf A Physicochem Eng Asp 436:1175–1185

[54] Patel VR, Agrawal YK (2011) Nanosuspension: an approach to enhance solubility of drugs. J Adv Pharm Technol Res 2:81–87

[55] Bhattacharjee S (2016) DLS and zeta potential-What they are and what they are not? J Control Release 235:337–351

[56] Luo YL, Yang XL, Xu F, Chen YS, Zhao X (2014) pH-triggered PMAA-*b*-HTPB-*b*-PMAA copolymer micelles: physicochemical characterization and camptothecin release. Colloid Polym Sci 292:1061–1072

[57] Guo QH, Zhang CJ, Wei C, Xu MM, Yuan YX, Gu RA, Yao JL (2016) Controlling dynamic SERS hot spots on a monolayer film of Fe_3O_4@Au nanoparticles by a magnetic field. Spectrochim Acta Part A Mol Biomol Spectrosc 152:336–342

[58] Guo M, Yan Y, Zhang H, Yan H, Cao Y, Liu K, Wan S, Huang J, Yue W (2008) Magnetic and pH-responsive nanocarriers with multilayer core–shell architecture for anticancer drug delivery. J Mater Chem 18:5104–5112

[59] Toor SK, Devi P, Bansod BS (2015) Electrochemical detection of trace amount of arsenic (III) at glassy carbon electrode modified with Au/Fe_3O_4 nanocomposites. Aquat Proc 4:1107–1113

[60] Han Q, Shen X, Zhu W, Zhu C, Zhou X, Jiang H (2016) Magnetic sensing film based on Fe_3O_4@Au-GSH molecularly imprinted polymers for the electrochemical detection of estradiol. Biosens Bioelectron 79:180–186

[61] Sanaeifar N, Rabiee M, Abdolranhim M, Tahriri M, Vashaee D, Tayebi L (2016) A novel electrochemical biosensor based on Fe_3O_4 nanoparticles-polyvinyl alcohol composite for sensitive detection of glucose. Anal Biochem 519:19–26

[62] Ghimire G, Yi Y, Derylo MA, Baker LA, Ito T (2015) Electron propagation within redox-active microdomains in thin films of ferrocene-containing diblock copolymers. Langmuir 31:12307–12314

[63] Cuadrado R, Puerta JM, Soria F, Cerdá JI (2013) A first principles study of thiol-capped Au nanoparticles: structural, electronic, and magnetic properties as a function of thiol coverage. J Chem Phys 139:034319

[64] Dutta P, Pal S, Seehra MS, Anand A, Roberts CB (2007) Magnetism in dodecanethiol-capped gold nanoparticles: role of size and capping agent. Appl Phys Lett 90:213102

[65] Zhang L (2009) The research on preparation and magnetic properties of gold nanoparticles. Master thesis, Huazhong University of Science & Technology

[66] Grau-Atienza A, Serrano E, Linares N, Svedlindh P, Seisenbaeva G, García-Martínez J (2016) Magnetically separable mesoporous Fe_3O_4/silica catalysts with very low Fe_3O_4 content. J Solid State Chem 237:138–143